

Atomistic modeling of diffusion processes at Al(Si)/Si(111) interphase boundaries obtained by vapor deposition

Yang Li, Raj K. Koju and Yuri Mishin

November 5, 2024

Department of Physics and Astronomy, MSN 3F3, George Mason University, Fairfax, Virginia 22030, USA

Abstract

Molecular dynamics and parallel-replica dynamics simulations are applied to investigate the atomic structures and diffusion processes at Al{111} || Si{111} interphase boundaries constructed by simulated vapor deposition of Al(Si) alloy on Si(111) substrates. Different orientation relationships and interface structures are obtained for different pre-deposition Si (111) surface reconstructions. Diffusion of both Al and Si atoms at the interfaces is calculated and compared with diffusion along grain boundaries, triple junctions, contact lines, and threading dislocations in the Al-Si system. It is found that Al{111} || Si{111} interphase boundaries exhibit the lowest diffusivity among these structures and are closest to the lattice diffusivity. In most cases (except for the Si substrate), Si atoms are more mobile than Al atoms. The diffusion processes are typically mediated by Al vacancies and Si interstitial atoms migrating by either direct or indirect interstitial mechanisms.

Keywords: Interfaces, diffusion, modeling, simulation, Al-Si system.

1 Introduction

Diffusion along metal-nonmetal interfaces plays an important role in many processes, such as phase transformations, diffusional creep in composite materials, and microstructure

development. Despite the practical significance, the fundamental understanding of diffusion in metal-nonmetal interfaces remains highly incomplete. Experimental investigations of interphase boundary diffusion are extremely challenging and reliable information is scarce. There have been very few measurements for metal-nonmetal systems [1–4], most of which are indirect. In particular, there have been no direct or indirect diffusion measurements for Al-Si interphase boundaries. Meanwhile, this system presents significant interest in the context of Al-Si composite alloys and as a model system to understand the phenomenon of interfacial creep in metal-matrix composites [5–9].

Previous research [10, 11] applied atomistic simulation methods to compute Al-Si interface diffusion coefficients and understand the underlying diffusion mechanisms. A critical step in such studies is to construct interfaces that remain structurally stable during high-temperature anneals required for diffusion calculations. In [10, 11], the interfaces were constructed by either bonding Si and Al single crystals with pre-determined crystallographic orientations, or by solidifying a liquid Al(Si) alloy on a Si substrate. Some of the stable orientation relationships discovered in [10, 11] had been previously observed in epitaxy experiments. Unfortunately, diffusion of Al and Si in the stable Al-Si interfaces was found to be too slow to quantify by conventional molecular dynamics (MD) simulations. Interface disconnections accelerated the interface diffusion, enabling calculations of diffusion coefficients. These turned out to be much smaller compared to grain boundary (GB) diffusion in Al. However, the intrinsic interface diffusivity in the absence of extrinsic defects remained beyond the reach of the MD methodology.

In this paper, we report on new atomistic simulations addressing the above limitation and providing a clearer picture of where the Al-Si interfaces belong in the hierarchy of diffusion pathways in materials. We focus on Al(Si){111} || Si{111} interfaces created by simulated vapor deposition. We show that the orientation relationship and interface structure depend on the pre-deposition reconstruction of the Si(111) surface. In all cases studied, the interface remains stable during the subsequent anneals at all temperatures up to the eutectic point. In contrast to previous work [10, 11], we combine conventional MD with the parallel replica dynamics method, which has allowed us to evaluate the *intrinsic* interface diffusivity and gain insights into the interface diffusion mechanisms. Furthermore, we have been able to calculate the diffusion coefficients in GBs, triple junctions, contact lines, and dislocations in the *same* system. This has enabled us to compare the Al-Si interface diffusivities with those in other short-circuit diffusion paths as well as the lattice of the Al(Si) alloy. The results indicate that the interphase diffusivity, at least in the Al{111} || Si{111} system, is extremely low and closest to the lattice diffusivity in the ranking of different diffusion pathways.

2 Methodology

2.1 Vapor deposition simulations

The Al/Si interphase boundaries (IPBs) were constructed through MD simulations mimicking epitaxy experiments. The MD simulations were conducted using the Large-scale Atomic/Molecular Massively Parallel Simulator (LAMMPS) [12]. The interatomic potential developed by Saidi et al. [13] was used to describe the chemical bonding in the binary Al-Si system. An Al(Si) alloy layer was deposited onto a Si(111) surface with either the unreconstructed 1×1 or reconstructed 7×7 atomic structure. The surface area of the substrate was of $22\times 19\text{ nm}^2$ for the 7×7 reconstructed surface and $42\times 42\text{ nm}^2$ for the 1×1 reconstructed surface.

Figure 1 explains the deposition setup using an example of an $\text{Al}_{0.93}\text{Si}_{0.07}$ layer growing on the Si(111) substrate at the growth temperature of 622 K. Prior to deposition, the substrate had a 7×7 reconstructed surface structure and a thickness of 5 nm. It had a thermally expanded lattice parameter corresponding to the growth temperature. The bottom two crystal planes of the substrate were fixed. Periodic boundary conditions (PBCs) were applied in the lateral directions X and Y with a fixed boundary condition along the growth direction Z . Al and Si atoms with a chosen Al:Si ratio were randomly created in a region (“gas”) well above the substrate surface. The atomic velocities were towards to the substrate and had magnitudes drawn from the Maxwell velocity distribution at the growth temperature. The atoms hitting the substrate were gradually building an Al(Si) alloy layer of the gas composition. This process produced an Al(Si)/Si IPB with the chosen crystallographic orientation of the substrate. Note that the simulation setup did not imposed any particular crystallographic orientation of the Al(Si) layer. The growing layer was free to choose the most favorite orientation during the growth process. The alloy composition and temperature were chosen so as to keep the alloy within the single-phase region on the left of the solvus line on the Al-Si phase diagram [10] computed with the interatomic potential.

We investigated the Al(Si)/Si IPBs at four temperatures: 578 K, 604 K, 622 K, and 638 K. These temperatures are close to the eutectic temperature (approximately 677 K) predicted by the interatomic potential. The corresponding solubility limits of Si in Al at these temperatures are 3.5%, 5.0%, 6.8%, and 8.0%. (In this work, all chemical compositions are measured in atomic per cents.) The deposition simulations targeted chemical compositions close to the solubility limits at the respective temperatures. The growth rate was around 0.1 monolayer per nanosecond (ML/ns). Due to the time scale limitation of MD simulations, this rate is several orders of magnitude higher than typical experimen-

tal growth rates, which are several ML/s. To partially mitigate the effect of the high growth rate, the first 2 MLs of the Al(Si) alloy were deposited on the 1×1 substrate with a relatively low rate of $0.7 \text{ ML}/\mu\text{s}$ at temperatures ranging from 578 to 638 K. For the 7×7 reconstructed surface, the first 2 MLs were deposited with the same $0.7 \text{ ML}/\mu\text{s}$ rate but at a higher temperature of 770 K to accelerate the structural rearrangement to the 1×1 reconstruction. The subsequent layers were grown at lower temperatures from 578 to 638 K. Using a raised temperature is a common strategy to mitigate the effects of a high growth rate [14–16]. Applying a slow deposition for the initial layers is also beneficial as the interface structure is largely determined during early stages of the growth process.

2.2 Diffusion coefficient calculations

In addition to Al(Si)/Si IPBs, a variety of microstructures formed in the Al(Si) layer during the depositions. The diffusion coefficients were computed for both the IPBs and these microstructures. Details of the diffusion calculations are presented below.

The self-diffusion coefficients of Al and Si in Al(Si)/Si IPBs were measured by tracking the motion of atoms within a 1.2 nm thick layer centered at the interface during the MD simulations in the canonical (NVT) ensemble. The 1.2 nm thickness approximately corresponds to three atomic layers of Si and three atomic layers of Al(Si). The choice of this thickness was based on the following. We computed the potential energy of atomic layers as a function of distance normal to the interface region and found that atoms within approximately 1.2 nm region centered at the IPB had potential energy significantly different from that in the bulk phases. The IPB position was determined by averaging the Z -coordinates of the interface atoms having non-lattice environments. The atomic environments were analyzed by the Polyhedral Template Matching (PTM) algorithm in the Open Visualization Tool OVITO [17].

The diffusion coefficients were calculated using the Einstein relations $D_x = \langle x^2 \rangle / 2t$ and $D_y = \langle y^2 \rangle / 2t$, where $\langle x^2 \rangle$ and $\langle y^2 \rangle$ are mean squared displacements (MSDs) of atoms in the two in-plane directions X and Y , and t is the simulation time. Only atoms that remained in the interface region at the initial and final times were included in the MSD calculation. In previous work [10, 11, 18], the diffusion coefficients were rescaled based on the fraction of locally disordered atoms within the interface region. This rescaling corrected for the possible underestimation of the diffusion coefficient when the fixed-width interface layer contained not only high-diffusivity pathways but also lattice-like atomic groups. Such groups did not contribute much to the diffusion flux and were excluded from the diffusion calculation. However, the IPBs studied in this work had very compact and largely uniform atomic structures (see examples in Fig. 2) that did not require such a rescaling.

For interfaces obtained by Al(Si) deposition on the Si(111)- 7×7 surface, the Al and Si diffusion coefficients were below 10^{-13} m²/s, which is close to the lower bound of measurable diffusivities in conventional MD simulations. Therefore, we applied the parallel replica dynamics (PRD) method [19, 20], which is one of the accelerated MD approaches [21]. The statistics of diffusive jumps detected by PRD allowed us to quantify the diffusion coefficients. Furthermore, the method identified typical atomic rearrangements causing the atomic diffusion. The activation barriers of such rearrangements were then computed by the nudged elastic band (NEB) method [22, 23]. The PRD calculations provided insights into diffusion mechanisms in the defect core regions, which would be difficult to obtain by other methods. Technical details of the PRD calculations are summarized in the Supplementary Information file accompanying this article.

Similar to the IPBs, self-diffusion coefficients of Al and Si in GBs were computed by tracking the motion of atoms within a 2.0 nm probe layer centered at the boundary during the MD simulations. The layer was thicker than for the IPBs because the GBs had less ordered structures with a thicker core region. After using the Einstein relations to calculate the diffusion coefficients, the results were rescaled by a factor equal to the ratio of the total number of atoms in the probe layer to the number of locally disordered atoms identified by PTM analysis in OVITO. The same methodology was used to compute the diffusion coefficients of GB triple junctions (GBTJs) and IPB-GB triple lines (GBTLs). For GBTJs, we tracked atoms in the common region of the three GBs connected to the GBTJ. The region had a cylindrical shape with a radius of 2 nm. For GBTLs, we tracked atoms in the common region of the GB and the IPB, which had a rectangular shape with a height of 1.2 nm (Z -direction) and a width of 2 nm (parallel to the interface). The diffusion coefficients were calculated from the Einstein relation and rescaled by the ratio of the total number of atoms in the region to the number of locally disordered atoms.

In addition to IPBs, GBs, and their triple lines, threading dislocations (TDs) formed in the growing Al(Si) layer during the deposition. Such dislocations were connected to the IPB at one end and to the open surface at the other end. To compute the diffusion coefficients in the dislocation cores, we tracked the motion of atoms within a cylindrical region whose axis was parallel to the Z direction. The radius of the cylinder was chosen to completely contain the TD core. As above, the diffusion coefficients were extracted from the Einstein relation followed by rescaling by the fraction of disordered atoms.

For all diffusion coefficients calculated in this study, bootstrap resampling of MSD curves was applied to compute error estimates. The hyper-parameters chosen for this calculation were a block length of 20 ps and a number of resampled trajectories equal to 100.

3 Results

3.1 Effect of Si(111) surface structure on the Al(Si)/Si(111) interphase boundary

The Si(111) surface structure can undergo several reconstructions [24–29]. In this work, we investigated the two most common surface structures corresponding to the 1×1 and 7×7 reconstructions. For brevity, we refer to the IPBs obtained by Al(Si) deposition onto the Si(111)- 1×1 and Si(111)- 7×7 substrates as (1×1) IPB and (7×7) IPB, respectively.

The simulations revealed two common features of the (1×1) and (7×7) IPB cases. Firstly, the Al(Si) growth followed the layer-by-layer mechanism in both cases. Secondly, the $[111]$ crystallographic direction in the deposited Al(Si) layer was always parallel to the growth direction Z , regardless of the growth temperature or Si concentration (Fig. 2). Thus, the obtained orientation relationship across the IPB was $\text{Al(Si)}\{111\} \parallel \text{Si}\{111\}$. However, differences were observed between the two IPB structures, as discussed below.

3.1.1 (1×1) interphase boundary

The (1×1) IPBs were found to be atomically sharp with very little intermixing between Al and Si. Simulations revealed two possible in-plane orientations at (1×1) IPBs. Namely, the $[0\bar{1}1]$ direction in the Al(Si) layer was rotated either $+19^\circ$ or -19° away from the $[0\bar{1}1]$ direction of the Si substrate. Different grains in Al(Si) exhibited one of these two orientations, as illustrated in Fig. 3. Each of the two orientations could additionally exhibit two different stacking sequences of the Al(Si) planes at the interface: either A-B-C or A-C-B. While both sequences represent the FCC structure, they were rotated relative to each other by about 70.5° about the common tilt axis $[110]$. The two in-plane rotations and the two stacking orders gave rise to four different grain orientations of the Al(Si) layer, which were all observed in the deposition simulations.

Fig. 4 shows typical polycrystalline structures of the Al(Si) layers deposited on Si(111)- 1×1 . The structures are composed of columnar grains with the common $[111]$ axis normal to the substrate. While specific grain shapes and sizes depended on the deposition temperature and chemical composition, all structures contained GBs, triple-line defects, and dislocations. Three types of GBs were observed: $\Sigma 3 \langle 110 \rangle$ 70.5° tilt GB (incoherent twin boundary), $\Sigma 7 \langle 111 \rangle$ 38.2° tilt GB, and $\Sigma 21 \langle 111 \rangle$ 21.8° tilt GB. As an example, in Fig. 5(a) we show a GBTJ connected to $\Sigma 3$, $\Sigma 7$, and $\Sigma 21$ GBs. The GBTJ is normal to the page, while the three GBTLs (GB/IPB intersections) are revealed as loci of non-FCC atoms. The $\Sigma 3$ incoherent twin GB is formed between two grains with similar in-plane orientations but

different stacking orders. A side view of this boundary is shown in Fig. 5(b).

We were unable to compare the simulation results for the (1×1) IPBs with experimental observations. To our knowledge, epitaxial growth of Al on Si(111)- 1×1 is difficult to implement. High-temperature annealing to remove the surface oxide renders the Si(111)- 1×1 surface unstable and causes its reconstruction to other surface structures [30]. This explains the lack of clear-cut experimental results for the (1×1) IPB structures.

3.1.2 (7×7) interphase boundary

The (7×7) IPB exhibits a cube-on-cube orientation relationship, in which the Al(Si) layer has its $[0\bar{1}1]$ and $[2\bar{1}\bar{1}]$ directions parallel to the $[0\bar{1}1]$ and $[2\bar{1}\bar{1}]$ directions of the Si substrate (Fig. 2(b)). The deposition temperature has little effect on the interface structure. Simulations show that the Si(111)- 7×7 surface undergoes a structural rearrangement during the Al(Si) deposition. Specifically, the dimer-atom-stacking fault structure of this surface [29] transforms into the Si(111)- 1×1 structure. This results in the orientation relationship $\text{Al(Si)}\{111\} \parallel \text{Si}\{111\}$ with $\text{Al(Si)}\langle 110 \rangle \parallel \text{Si}\langle 110 \rangle$. Note that this orientation relationship differs from the one obtained by depositing Al(Si) directly on the Si(111)- 1×1 surface, in which case the $\text{Al(Si)}\langle 110 \rangle$ and $\text{Si}\langle 110 \rangle$ axes are misaligned by $\pm 19^\circ$ (see above). Another distinct feature of the Si(111)- 7×7 deposition is some intermixing between the Al and Si atoms in the interface region, which was not observed in the (1×1) IPBs. The intermixed Al atoms are constrained to the first layer of the Si substrate adjacent to the IPB. This intermixing is coupled to the structural rearrangement occurring on the surface of the Si substrate. (The described intermixing is not apparent in Fig. 2(b) because it only shows a small interface area.)

The simulation results agree well with the experimental interface structures obtained by growing Al thin films on Si(111)- 7×7 substrates by molecular beam epitaxy [30, 31]. The epitaxy experiments reveal the same orientation relationship and a similar structural transformation of the Si surface as found in the simulations. Both simulations and experiments indicate that the initial Si surface reconstruction significantly impacts the orientation relationship across the Al(Si)/Si interface obtained by vapor deposition.

The simulations have also shown that the Al(Si) layers deposited on the Si(111)- 7×7 substrates are single-crystalline. This observation is consistent with the experimental observation of very low GB density (significantly less than $1 \mu\text{m}^{-1}$) in Al layers deposited on Si(111)- 7×7 substrates [31]. Such a low GB density is unlikely to be captured by MD deposition simulations, which are limited to the ~ 10 nm length scale.

3.2 Diffusion coefficients from conventional MD simulations

Next, we present the calculation results for Al and Si diffusion along the IPBs and other defects in the microstructure of the Al(Si)/Si system. These results were obtained by conventional MD simulations.

Fig. 6 shows a typical microstructure formed by deposition on the Si(111)- 1×1 substrate. The diffusion coefficients were computed using the methodology discussed in Section 2.2, which is based on Einstein’s formula for MSDs of atoms. Typical MSD versus time plots are shown in Fig. 7. In most cases, the predicted linear relation is followed fairly well, although deviations from linearity were also observed. At least two factors could be responsible for such deviations. The first factor is the spatial heterogeneity of the diffusion pathways. For example, atoms near the center of the interface core usually possess a higher mobility than atoms in distorted lattice planes immediately adjacent to the interface. Since both are included in the MSD calculation, deviations from the Einstein relation (which assumes a homogeneous medium) are inevitable. They can accumulate with time, leading to a nonlinear behavior at longer times. The second factor is that the MSD calculation only includes atoms that remained within the probe region during the chosen time interval. Higher-mobility atoms are more likely to leave the probe region and not contribute to the MSD. This leads to underestimated MSDs, causing downward deviations from the linearity of the MSD-time plots in the long-time limit. When a plot deviated from linear behavior, we used its initial (short-time) part to extract the diffusion coefficient.

In Fig. 8, we present the Arrhenius diagrams (log diffusivity versus inverse temperature) for the Al and Si diffusion coefficients in the defect structures. Recall that at each temperature, the chemical composition of the Al(Si) alloy corresponds to the thermodynamic equilibrium between the phases at that temperature. In other words, the chemical composition varies with temperature. The main results of the calculations are summarized below.

For IPBs and GBs, the diffusivity tends to decrease in the order: (Si in $\Sigma 7$ GB) > (Si in $\Sigma 21$ GB) > (Al in $\Sigma 7$ GB) > (Al in $\Sigma 21$ GB) \approx (Si in $\Sigma 3$ GB) > (Al in $\Sigma 3$ GB) > (Si in Al(Si) at (1×1) IPB) > (Al in (1×1) IPB) > (Si in (1×1) IPB) (Fig. 8). Overall, GBs exhibit much higher diffusivity than IPBs, with the difference reaching about two orders of magnitude. Among the GBs, the $\Sigma 7$ GB has the highest diffusivity and the $\Sigma 3$ GB the lowest. This trend correlates with the strength of Si GB segregation: the $\Sigma 7$ GB exhibits the highest Si segregation and the $\Sigma 3$ GB the lowest. (The results for Si GB segregation are presented in the Supplementary Information file.) The diffusion coefficients in the (1×1) IPBs are near the lower limit of diffusion coefficients measurable by conventional MD simulations (around 10^{-13} m²/s). The diffusion coefficients of Si and Al in the (7×7)

IPB are below this limit and are not shown in Fig. 8.

Si exhibits a higher GB diffusivity than Al, which is consistent with previous work [10, 11]. In contrast, Si diffusivity in the IPBs is consistently lower than Al diffusivity. This trend was also noted in [10, 11] and was explained by the ordering effect imposed by the Si substrate. Indeed, at the temperatures studied here, the Si atoms in the substrate are virtually immobile. Their highly ordered spatial arrangement imposes a period constraint on the IPB atoms, reducing their mobility. To verify this effect, we recomputed the diffusion coefficients of Si in the (1×1) and (7×7) IPBs by excluding the substrate Si atoms from the probe layer. Only Si atoms diffusing on the Al(Si) side of the interface region were included in the MSD calculations. The Si diffusion coefficients obtained were still much lower than those for GB diffusion but an order of magnitude higher than the diffusion coefficients computed by including all atoms within the probe layer (Fig. 8(b,c)). Furthermore, as shown on the Arrhenius diagram, Si diffusivity on the Al(Si) side of the IPBs is consistently higher than the Al diffusivity, which aligns with the proposed explanation.

The anisotropy of GB and IPB diffusion is relatively small. In most cases, it cannot be detected beyond the statistical scatter of the data points. The only cases where the anisotropy is likely to be statistically significant is for Si diffusion in the $\Sigma 3$ and $\Sigma 21$ GBs.

Si diffuses in GBTJs faster than Al, and both diffusivities are close to that in $\Sigma 7$ GBs (Fig. 8d). This observation suggests that the GBTJ diffusivity is governed by the highest-diffusivity GB connected to the junction. Al diffusivity in GBTLs correlates with the respective GB diffusivity and decreases in the order ($\Sigma 7$ GB) > ($\Sigma 21$ GB) > ($\Sigma 3$ GB). Si diffusion in GBTLs is too slow to be quantified because many Si atoms in the GBTL belong to the top substrate layer and are virtually immobile. Al diffusion along disconnection loops in the (1×1) IPB is on the order of 10^{-13} m²/s (Fig. 8(d)), while Si diffusion is too slow to be measured. Thus, diffusion in the (1×1) IPB is dominated by GBTLs.

3.3 Simulations by parallel replica dynamics

3.3.1 Investigation of diffusion mechanisms

As discussed above, calculations of the diffusion coefficients in the (7×7) IPB are below the capabilities of conventional MD simulations. The same is true for diffusion in the (1×1) IPB outside the GBTLs and disconnection loops. To overcome this limitation, we applied the PRD method [19, 20] at temperatures ranging from 578 K to 638 K to estimate the IPB diffusivities and gain insights into the diffusion mechanisms.

The deposited Al(Si)/Si systems were too large for PRD simulations. Instead, we con-

structured a set of relatively small fully periodic models mimicking the deposited structures. To model the (7×7) IPB, the $[0\bar{1}1]$ and $[2\bar{1}\bar{1}]$ directions in the Al(Si) layer were aligned parallel to those in the substrate (Fig. 9(a)). Due to the PBCs, the model effectively contained two IPBs. The substrate contained 216 Si atoms and the Al(Si) layer contained 384 atoms. To represent the (1×1) IPB, the $[0\bar{1}1]$ and $[2\bar{1}\bar{1}]$ directions in Al(Si) were misaligned by approximately 19° relative to those in the Si substrate. In this case, the substrate contained 288 Si atoms and the Al(Si) layer contained 504 atoms. In both cases, the system dimensions and the numbers of atoms were adjusted to satisfy the PBCs. For comparison, we also constructed a set of single-phase Al(Si) structures containing 216 atoms, as illustrated in Fig. 9(b). In all cases, the Si concentration in Al(Si) ranged from approximately 3.5% to 8%, matching the estimated solid solubility of Si in Al along the solvus line on the phase diagram.

The initial structures did not contain any point defects, and PRD detected very few diffusive events. This is not surprising because the deposited structures contained vacancies and interstitial atoms responsible for diffusion activity. Therefore, we next introduced an interstitial or a vacancy in the models. The results are summarized below.

An Al vacancy diffuses primarily by exchanges with Al atoms, regardless of the Si concentration in Al(Si) (Fig. 10a). Even in systems containing 8% of Si in Al(Si), PRD detected over a thousand vacancy-Al exchanges and only a few vacancy exchanges with Si atoms. Very few Al self-interstitials were observed. When an interstitial Al atom was introduced into the model prior to the PRD simulation, it typically kicked a substitutional Si atom out of its position and took its place, creating a Si interstitial.

The diffusion behavior of Si atoms is more complex. Si interstitial atoms in Al(Si) were found in three different configurations: $\langle 100 \rangle$ dumbbell (two Si atoms aligning parallel to the $\langle 100 \rangle$ crystallographic direction sharing a lattice site), tetrahedral configuration, and octahedral configuration. Octahedral interstitials were observed least frequently. Si atoms diffused by either the direct interstitial mechanism or the indirect mechanism called the interstitialcy mechanism. In the first case, the interstitial Si atom hops directly to a neighboring interstitial position without displacing lattice atoms. Most of the time, the atom hops between tetrahedral interstitial sites (Fig. 10b). Note that only Si atoms participate in this process, causing no Al diffusion. In the interstitialcy events, multiple atoms move simultaneously, forming a structural excitation causing a collective string-like atomic displacement of several atoms (Fig. 10c). The event typically, starts with a Si interstitial atom jumping into a neighboring lattice site, displacing the resident atom into an adjacent interstitial position. The displaced atom, in turn, displaces another atom from its substitutional position, and the displacement process continues. This chain of

displacements typically ends with the formation of a new Si interstitial. Note that both Al and Si atoms can participate in the interstitialcy mechanism, causing diffusion of both species. With increasing Si concentration in Al(Si), the Si interstitials are more likely to diffuse by the interstitialcy mechanism rather than the direct interstitial mechanism in both the interface regions and the lattice.

Fig. 10 illustrates the diffusion mechanisms mentioned above and the respective NEB minimum energy paths in the (1×1) and (7×7) IPB regions and the Al(Si) lattice. In all three cases, the diffusion mechanisms are qualitatively similar. Thus, we do not find a unique mechanism of IPB diffusion. However, the energy barriers in the interface region are lower than in the lattice. The energy difference ranges from a few hundredths to a few tenths of eV and is responsible for the accelerated diffusion in the interfaces relative to the lattice.

3.3.2 Diffusion coefficients from parallel replica dynamics

Figure 11 shows the Al and Si diffusion coefficients obtained by the PRD simulations. Since the diffusion coefficients in the (7×7) and (1×1) IPBs (unaffected by GBTLs) are quite similar, we will discuss them collectively as interface diffusion. The diffusion calculations in PRD are based on the transition events detected by the method, which involve only part of the atoms located in the chosen probe region. Considering only the diffusing atoms (i.e., those which participate in diffusion events) allows us to identify the diffusion mechanisms and rank their rates. However, this approach significantly overestimates the diffusion coefficients because only the most frequent events are counted. Considering all atoms in the probe region provides more accurate diffusion coefficients but rescales the contributions of the individual diffusion mechanisms to the overall diffusivity according to fractions of the respective defects in the chosen region. Both approaches were considered in this work.

Including only the diffusing atoms (Fig. 11b,d), the diffusivity decreases in the order (interface and lattice Al by the vacancy mechanism) > (interface Al and Si by the interstitial mechanism) > (lattice Al and Si by the interstitial mechanism). For brevity, by the interstitial mechanism we mean both the direct and the interstitialcy mechanisms. The results suggest that diffusion by Al vacancies is the fastest process. Furthermore, as predicted by the NEB calculations, both Al and Si atoms diffuse faster in the interface region than in the lattice, although the difference is less than an order of magnitude. The diffusivities of Al and Si by the interstitial/interstitialcy mechanism are close to each other, which is also consistent with the NEB calculations showing that the Si and Al diffusion barriers of interstitial/interstitialcy events are similar.

Considering all atoms in the interface and lattice regions, all diffusion coefficients become significantly smaller than in the previous case, but they could still be measured by PRD (Fig. 11a,c). The diffusivity decreases in the order (interface Si by the interstitial mechanism) > (lattice Si by the interstitial mechanism) > (interface Al by the interstitial mechanism) > (lattice and interface Al by the vacancy mechanism) > (lattice Al by the interstitial mechanism). As above, interface diffusion is faster than lattice diffusion. However, the Si diffusion coefficients are now larger than those of Al diffusion. The effect is primarily due to the larger number of interstitials in the deposited Al(Si)/Si layer compared to vacancies, with the difference reaching a factor of 20 to 30 (see Supplementary Information for details of the point-defect computations). Another factor is that the probe region now contains more non-diffusing Al atoms than Si atoms, which further reduces the measured Al diffusivity. Note that there is no significant diffusion anisotropy of Al or Si atoms in the interface region or the lattice.

4 Conclusions

We have performed an MD simulation study of Al and Si diffusion in Al(Si){111} || Si{111} IPBs created by simulated vapor deposition. Besides the IPBs, the deposited Al(Si) layers contain other structural elements, including GBs, GBTLs, GBTJs, TDs, and disconnections. The diffusivity in all these structures has been computed for comparison with IPBs. We find that the IPB diffusivity is too low to be measured by conventional MD simulations. Previous work [10, 11] arrived at a similar conclusion. Therefore, we have applied the PRD method to investigate the diffusion mechanisms and quantify the IPB diffusion coefficients. The main conclusions of this work can be summarized as follows:

1. The Si surface reconstruction prior to the Al(Si) deposition affects the obtained IPBs. The Si(111)- 1×1 and Si(111)- 7×7 surface reconstructions give rise to different orientation relationships and different IPB structures.
2. It was previously suggested [32] that Al/Si (7×7) IPBs could be semi-coherent considering the significant lattice mismatch. Our simulations indicate that both the (1×1) and (7×7) IPBs have uniform incoherent structures. We observed no misfit dislocations at any chemical composition or temperature.
3. At all temperatures studied in this work, Si diffusion in the substrate is virtually frozen out. A few Al atoms penetrate into the Si substrate during the deposition process, but their concentration is too small to evaluate the diffusivity. In contrast,

the concentration of Si atoms in the deposited Al(Si) layer is higher and their diffusivity could be measured. We find that Si exhibits a higher diffusivity in Al(Si) than Al.

4. The Al and Si diffusion coefficients in the (1×1) and (7×7) IPBs are smaller than 10^{-13} m²/s at all temperatures studied here. They are only slightly higher than the lattice diffusion coefficients in Al(Si), with the difference being less than an order of magnitude. The IPB diffusion is dominated by the same interstitial and vacancy diffusion mechanisms as Al(Si) lattice diffusion. GBTLs in the (1×1) IPB can significantly accelerate the interface diffusion. No significant diffusion anisotropy was found in the IPBs.
5. All three types of GBs studied in this work (Σ 3, Σ 7, and Σ 21) exhibit higher diffusion coefficients than the Al{111} || Si{111} IPBs, with the difference being more than one order of magnitude. Si diffusion in the GBs is faster than Al diffusion. No significant diffusion anisotropy has been observed in the GBs.
6. The GBs form GBTLs when they intersect with IPBs. The GBTL diffusion closely correlates with the respective GB diffusion. If the GB has a higher diffusivity, so does the corresponding GBTL. Overall, GBTL diffusion is slower than the GB diffusion. GBTL diffusion is close to that of the GB with the highest diffusivity to which it is connected. Among the line defects, GBTLs exhibit a higher diffusivity than GBTLs and threading dislocations.

Acknowledgements

This research was supported by the U.S. Department of Energy, Office of Basic Energy Sciences, Division of Materials Sciences and Engineering, under Award # DE-SC0023102.

References

- [1] B. B. Straumal, L. M. Klinger, L. S. Shvindlerman, The effect of crystallographic parameters of interphase boundaries on their surface tension and parameters of the boundary diffusion, *Acta Metallurgica* 32 (1984) 1355–1364.
- [2] A. Kosinova, O. Kovalenko, L. Klinger, E. Rabkin, Mechanisms of solid-state dewetting of thin Au films in different annealing atmospheres, *Acta Materialia* 83 (2015) 91–101.

- [3] A. Kumar, H. Barda, L. Klinger, M. W. Finnis, V. Lordi, E. Rabkin, D. J. Srolovitz, Anomalous diffusion along metal/ceramic interfaces, *Nature Communications* 9 (2018) 5251.
- [4] H. Barda, E. Rabkin, Metal hetero-diffusion along the metal-ceramic interfaces: A case study of Au diffusion along the Ni-sapphire interface, *Acta Materialia* 186 (2020) 242–249.
- [5] J. V. Funn, I. Dutta, Creep behavior of interfaces in fiber reinforced metal–matrix composites, *Acta Materialia* 47 (1998) 149–164.
- [6] I. Dutta, Role of interfacial and matrix creep during thermal cycling of continuous fiber reinforced metal–matrix composites, *Acta Materialia* 48 (2000) 1055–1074.
- [7] K. A. Peterson, I. Dutta, M. W. Chen, Diffusionally accommodated interfacial sliding in metal-silicon systems, *Acta Materialia* 51 (2003) 2831–2846.
- [8] K. A. Peterson, I. Dutta, M. W. Chen, Measurement of creep kinetics at Al-Si interfaces, *Scripta Materialia* 47 (2002) 649–654.
- [9] K. A. Peterson, I. Dutta, M. Chen, Processing and characterization of diffusion-bonded Al-Si interfaces, *Journal of Materials Processing Technology* 145 (2004) 99–108.
- [10] I. Chesser, R. Koju, A. Vellore, Y. Mishin, Atomistic modeling of metal-nonmetal interphase boundary diffusion, *Acta Materialia* 257 (2023) 119172.
- [11] I. Chesser, R. K. Koju, Y. Mishin, Atomic-level mechanisms of short-circuit diffusion in materials, *International journal of materials research* 115 (2024) 85–105.
- [12] S. Plimpton, Fast parallel algorithms for short-range molecular-dynamics, *J. Comput. Phys.* 117 (1995) 1–19.
- [13] P. Saidi, T. Frolov, J. J. Hoyt, M. Asta, An angular embedded atom method interatomic potential for the aluminum–silicon system, *Modelling and Simulation in Materials Science and Engineering* 22 (2014) 055010.
- [14] J. Gruber, X. Zhou, R. Jones, S. Lee, G. Tucker, Molecular dynamics studies of defect formation during heteroepitaxial growth of InGa_N alloys on (0001) GaN surfaces, *Journal of applied physics* 121 (2017).

- [15] X. Zhou, D. Ward, J. Martin, F. Van Swol, J. Cruz-Campa, D. Zubia, Stillinger-weber potential for the ii-vi elements Zn-Cd-Hg-S-Se-Te, *Physical Review B* 88 (2013) 085309.
- [16] Y. Li, B. Gu, A. Diaz, S. R. Phillpot, D. L. McDowell, Y. Chen, Dislocation formation in the heteroepitaxial growth of PbSe/PbTe systems, *Acta Materialia* 260 (2023) 119308.
- [17] P. M. Larsen, S. Schmidt, J. Schiøtz, Robust structural identification via polyhedral template matching, *Modelling and Simulation in Materials Science and Engineering* 24 (2016) 055007.
- [18] I. Chesser, Y. Mishin, Point-defect avalanches mediate grain boundary diffusion, *Communications Materials* 3 (2022) 90.
- [19] A. F. Voter, Parallel replica method for dynamics of infrequent events, *Phys. Rev. B* 57 (1998) R13985–R13988.
- [20] D. Perez, B. P. Uberuaga, A. F. Voter, The parallel replica dynamics method – Coming of age, *Computational Materials Science* 100 (2015) 90–103.
- [21] D. Perez, B. P. Uberuaga, Y. Shim, J. G. Amar, A. F. Voter, Chapter 4 Accelerated Molecular Dynamics Methods: Introduction and Recent Developments, volume 5, Elsevier, 2009, pp. 79–98. doi:[https://doi.org/10.1016/S1574-1400\(09\)00504-0](https://doi.org/10.1016/S1574-1400(09)00504-0).
- [22] G. Henkelman, B. P. Uberuaga, H. Jónsson, A climbing image nudged elastic band method for finding saddle points and minimum energy paths, *J. Chem. Phys.* 113 (2000) 9901.
- [23] G. Henkelman, H. Jonsson, Improved tangent estimate in the nudged elastic band method for finding minimum energy paths and saddle points, *J. Chem. Phys.* 113 (2000) 9978–9985.
- [24] R. Becker, J. A. Golovchenko, E. McRae, B. Swartzentruber, Tunneling images of atomic steps on the Si (111) 7×7 surface, *Physical Review Letters* 55 (1985) 2028.
- [25] G. Binnig, H. Rohrer, C. Gerber, E. Weibel, 7×7 reconstruction on Si (111) resolved in real space, *Physical Review Letters* 50 (1983) 120.
- [26] K. D. Brommer, M. Needels, B. Larson, J. Joannopoulos, Ab initio theory of the Si (111)-(7×7) surface reconstruction: A challenge for massively parallel computation, *Physical Review Letters* 68 (1992) 1355.

- [27] M. Smeu, H. Guo, W. Ji, R. A. Wolkow, Electronic properties of Si (111)- 7×7 and related reconstructions: Density functional theory calculations, *Physical Review B* 85 (2012) 195315.
- [28] S. D. Solares, S. Dasgupta, P. A. Schultz, Y.-H. Kim, C. B. Musgrave, W. A. Goddard, Density functional theory study of the geometry, energetics, and reconstruction process of Si (111) surfaces, *Langmuir* 21 (2005) 12404–12414.
- [29] K. Takayanagi, Y. Tanishiro, S. Takahashi, M. Takahashi, Structure analysis of Si (111)- 7×7 reconstructed surface by transmission electron diffraction, *Surface science* 164 (1985) 367–392.
- [30] B. M. McSkimming, A. Alexander, M. H. Samuels, B. Arey, I. Arslan, C. J. Richardson, Metamorphic growth of relaxed single crystalline aluminum on silicon (111), *Journal of Vacuum Science & Technology A* 35 (2017).
- [31] X.-Y. Liu, I. Arslan, B. W. Arey, J. Hackley, V. Lordi, C. J. Richardson, Perfect strain relaxation in metamorphic epitaxial aluminum on silicon through primary and secondary interface misfit dislocation arrays, *ASC Nano* 12 (2018) 6843–6850.
- [32] W. Wu, M. Gong, B. Wei, A. Misra, J. Wang, Atomistic modeling of interface strengthening in Al-Si eutectic alloys, *Acta Materialia* 225 (2022) 117586.
- [33] R. K. Koju, Y. Mishin, Atomistic study of grain-boundary segregation and grain-boundary diffusion in Al-Mg alloys, *Acta Materialia* 201 (2020) 596–603.
- [34] A. Stukowski, Structure identification methods for atomistic simulations of crystalline materials, *Modelling and Simulation in Materials Science and Engineering* 20 (2012) 045021.

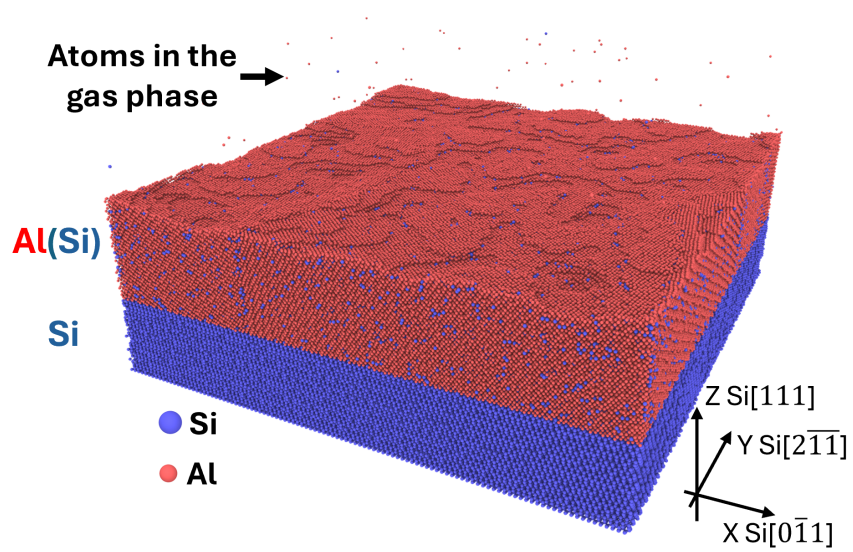


Figure 1: Simulated growth of $\text{Al}_{0.93}\text{Si}_{0.07}$ layer on $\text{Si}(111)$ substrate with 7×7 reconstructed surface by vapor deposition at the temperature of 622 K. The Cartesian X , Y , and Z directions are along the $[0\bar{1}1]$, $[2\bar{1}\bar{1}]$, and $[111]$ crystallographic directions of the substrate.

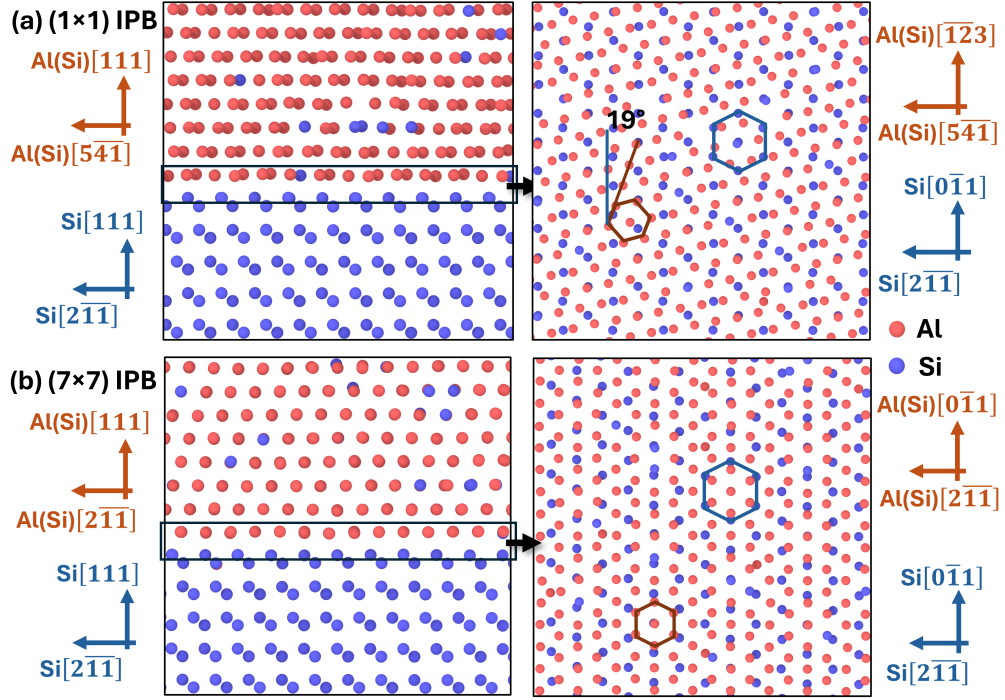


Figure 2: Structures of $\text{Al}_{0.92}\text{Si}_{0.08}(111)/\text{Si}(111)$ interphase boundaries obtained by vapor deposition at 638 K. Two orientation relationships and interface structures were obtained for different Si surface reconstructions: (a) (1×1) surface and (b) (7×7) surface. The left column shows side views of the interface structures. The right column shows a plane view of the top atomic layer of the Si substrate and the bottom atomic layer of $\text{Al}(\text{Si})$. Atoms in red and blue represent Al and Si atoms, respectively. The hexagons outline structural motifs.

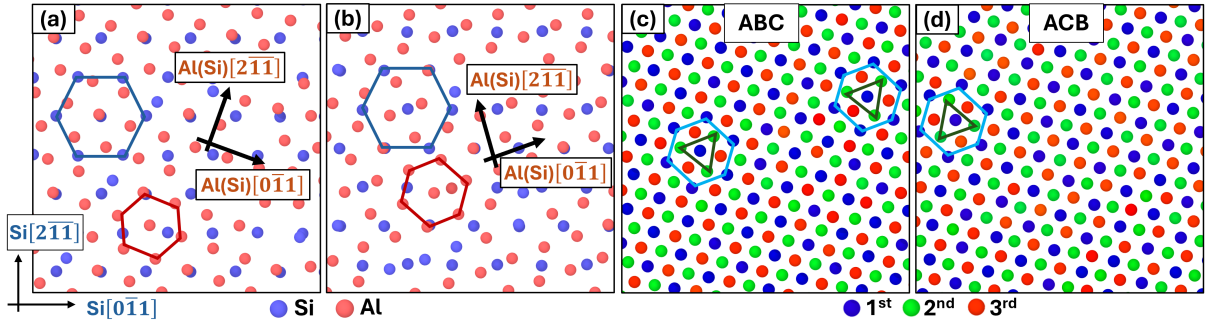


Figure 3: Panels (a) and (b) are plane views of the (1×1) IPB with two different orientation relationships. The top atomic layer of the Si substrate is superimposed on the bottom atomic layer of Al(Si). Panels (c) and (d) show three sequential atomic layers of Al(Si) found in different grains of the Al(Si) phase, illustrating two possible stacking orders: A-B-C and A-C-B. The bottom plane A is in immediate contact with the Si substrate. The atoms are colored according to their plane. The hexagons outline the structural motifs.

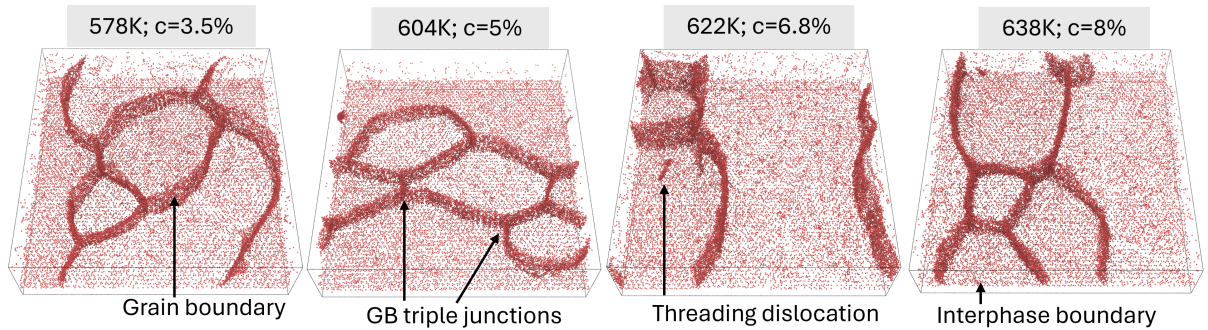


Figure 4: Perspective view of the Al(Si) layer deposited on Si(111)- 1×1 substrate at four temperatures ranging from 578 K to 638 K and Si concentrations c between 3.5% to 8.0%. Only atoms in locally disordered environments are shown to reveal IPBs, GBs, GBTLs, GBTJs, and threading dislocations.

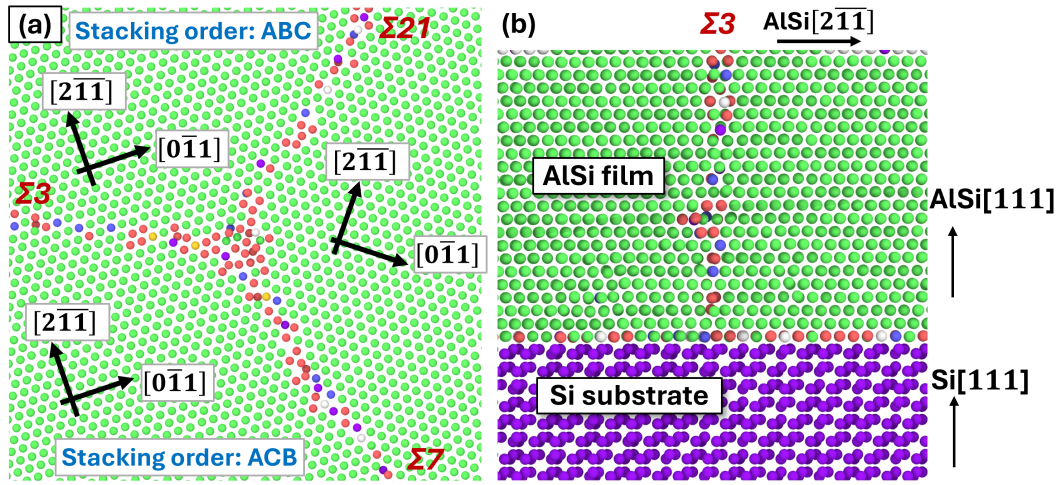


Figure 5: (a) Plane view of three grains in Al(Si) layer with the Si concentration of 8% deposited on Si(111)-1 \times 1 substrate at 638 K. The GBs and their triple junction are normal to the page. (b) Side view of this structure showing the $\Sigma 3$ incoherent twin boundary. The atoms are colored by local coordination number according to the scheme: green for FCC, purple for simple cubic, and all other colors represent atoms in locally disordered environments. The atoms at GBs and the IPB are red, grey, or blue.

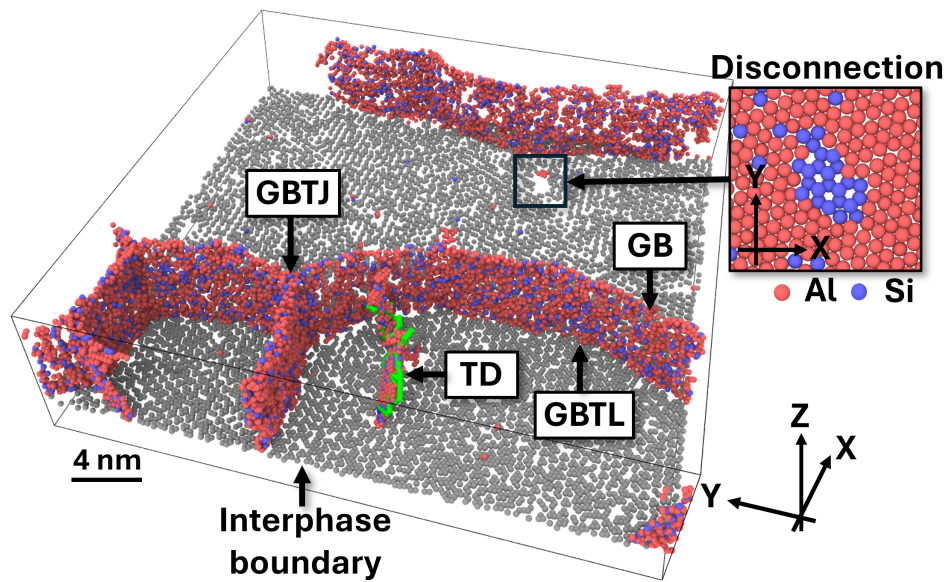


Figure 6: Perspective view of a polycrystalline $\text{Al}_{0.93}\text{Si}_{0.07}$ layer deposited on a $\text{Si}(111)\text{-}1\times 1$ substrate. The arrows point to defects used in diffusion calculations: interphase boundary (IPB), grain boundaries (GBs), grain boundary triple junctions (GBTJ), GB-IPB triple lines (GBTL), and threading dislocations (TD). The zoomed-in image shows a disconnection (DC) loop at the IPB, with the blue and red colors representing Si and Al atoms, respectively.

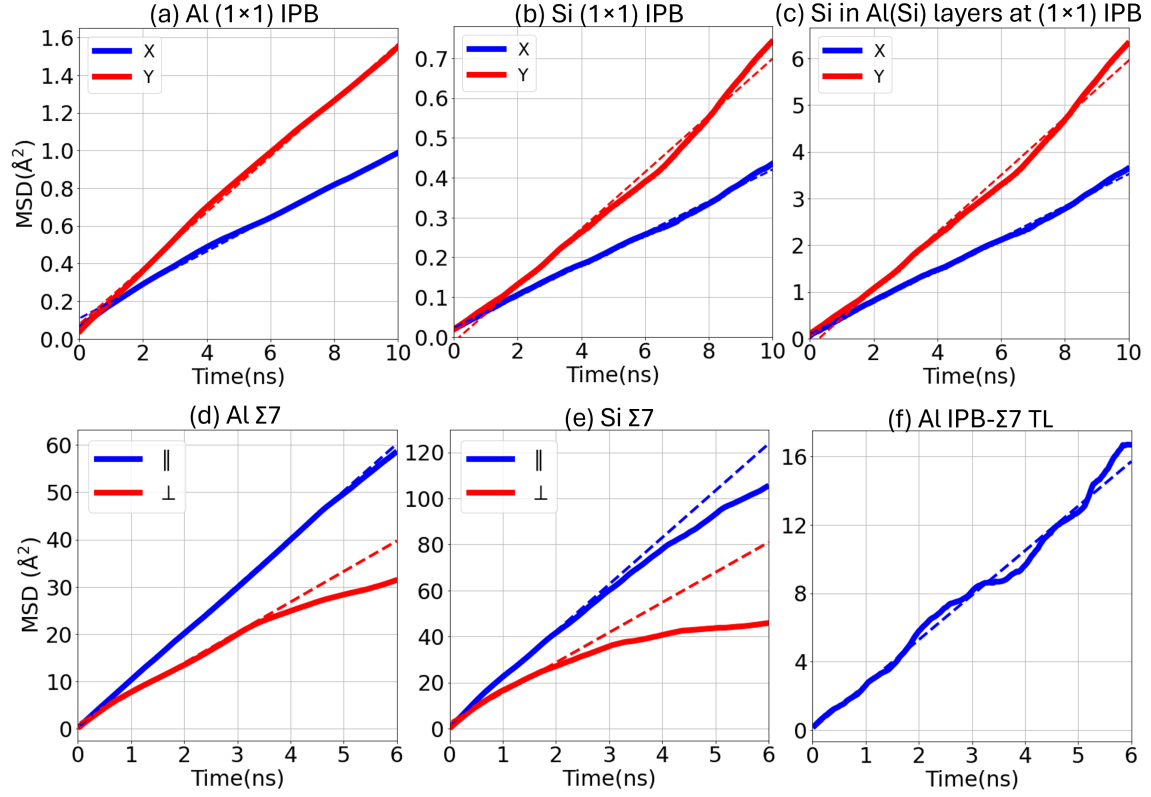


Figure 7: Representative MSD versus time plots obtained by MD simulations. (a,b) Al and Si atoms diffusing in the X and Y directions in the (1×1) IPB. (c) Si atoms diffusing in the (1×1) IPB excluding Si atoms in the substrate. (d,e) Al and Si atoms in a $\Sigma 7$ GB segment diffusing in directions parallel (\parallel) and normal (\perp) to the substrate. (f) Al atoms diffusing along a triple line between the (1×1) IPB the $\Sigma 7$ GB.

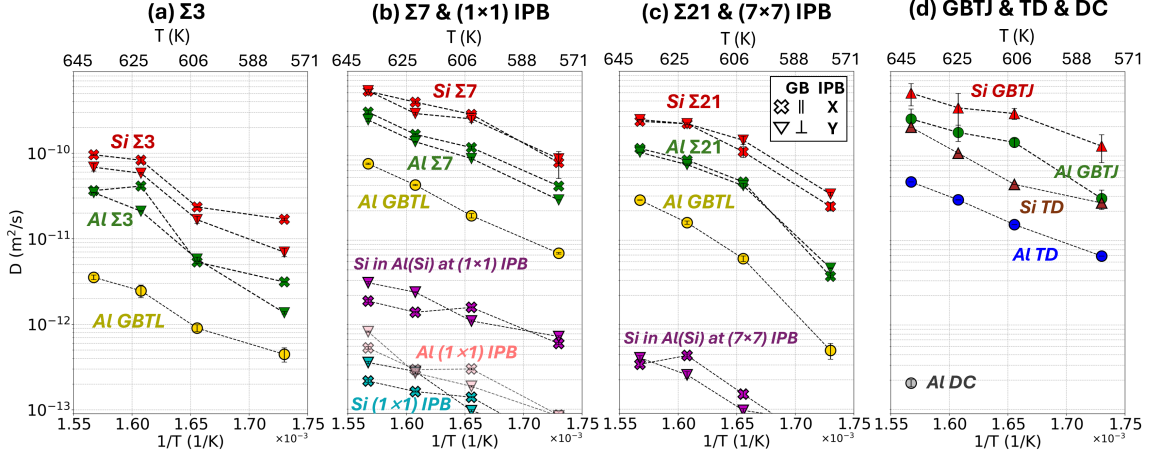


Figure 8: Arrhenius diagrams of Al and Si diffusion at the (a) $\Sigma 3$ GB, (b) $\Sigma 7$ GB and (1×1) IPB, (c) $\Sigma 21$ GB and (7×7) IPB. The Al diffusion coefficient at GBTLs is included for comparison. (d) Al and Si diffusion at GBTJs, TDs, and DC loops in the (1×1) IPB. The X and Y directions correspond to the $[0\bar{1}1]$ and $[2\bar{1}\bar{1}]$ directions of the Si substrate. The symbols \parallel and \perp refer to directions in the GB plane parallel and perpendicular to the IPB, respectively. For the $\Sigma 7$ and $\Sigma 21$ GBs, the \perp direction is aligned with the $[111]$ tilt axis.

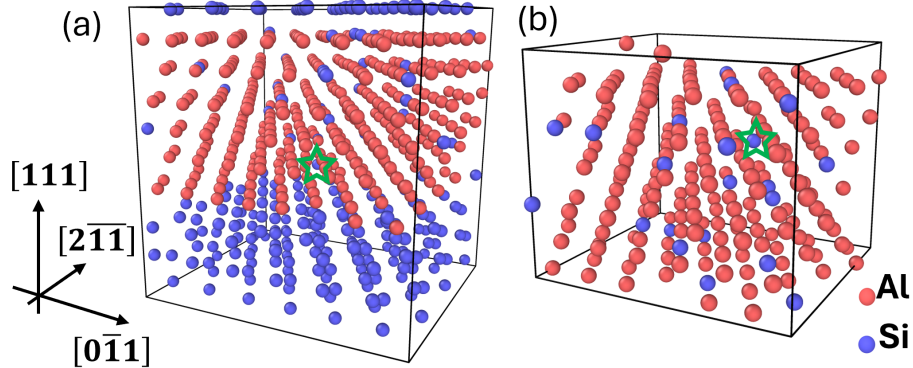


Figure 9: Small models prepared for PRD simulations. (a) Al(Si)/Si model representing a (7×7) IPB. (b) Single-crystalline Al(Si) model. The pentagons mark Si interstitials.

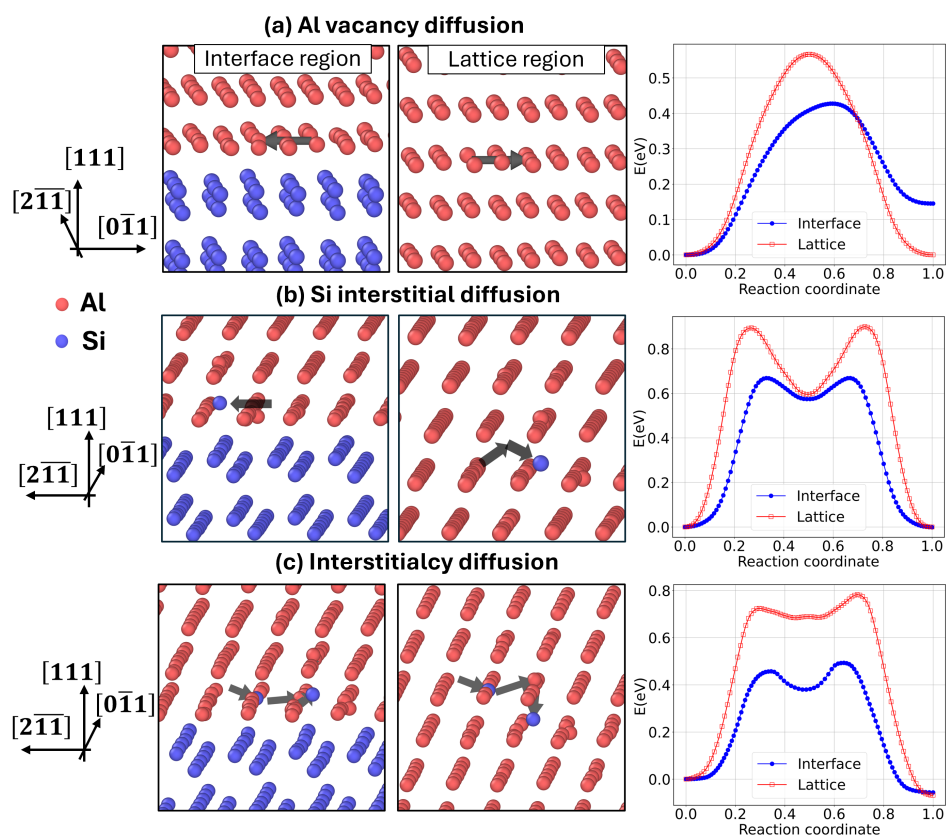


Figure 10: Illustration of diffusion mechanisms revealed by PRD simulations. (a) Al vacancy diffusion. (b) Direct Si interstitial mechanism. In the lattice, the Si interstitial jumps between tetrahedral sites. (c) Interstitialcy mechanism involving Si and Al atoms in the (7×7) interface and a lattice region. The arrows present atomic displacements. The third column presents selected minimum-energy paths obtained by NEB calculations.

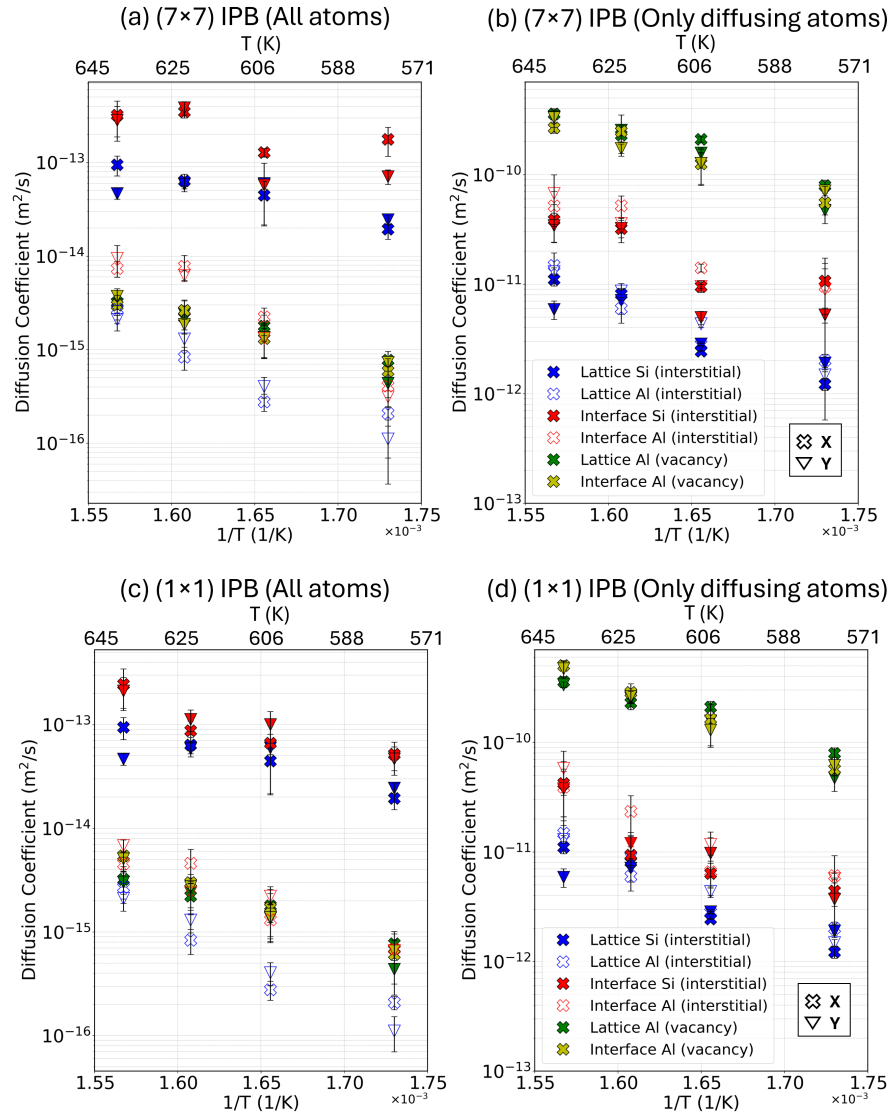


Figure 11: Diffusion coefficients for Al and Si atoms obtained by PRD calculations considering all atoms (a,c) and only diffusing atoms (b,d). The results for the (7×7) IPB and (1×1) are shown in (a,b) and (c,d), respectively.

SUPPLEMENTARY INFORMATION

5 Si segregation at grain boundaries

Si atoms strongly segregate to the grain boundaries (GBs) in Al(Si) deposited on the Si(111)-1×1 substrate. We computed the average Si concentration in different types of GBs in Al(Si) layers deposited at different temperatures. The results are shown in Fig. S1. The calculation was as follows [33]. We separated the GBs into 3 nm long segments in the interface plane. Each segment was 2 nm thick and was centered at the GB core. Then, we computed the number of Si and Al atoms in each segment. The amount of Si segregation $[N_{Si}]$ was quantified by the excess number of Si atoms per unit area A relative to the average Si concentration c in Al(Si):

$$[N_{Si}] = \frac{(N_{Si} - Nc)}{A}.$$

Here, N and N_{Si} denote the total number of atoms and the number of Si atoms within the GB segment, respectively. The results were averaged over all GB segments of the same type. The error bars in Fig. S1 represent the standard deviation from the average. As can be seen from Fig. S1, overall, $\Sigma 7$ boundaries exhibit the highest Si segregation, while $\Sigma 3$ boundaries the lowest. This order correlates with the GB diffusivities reported in the main text, where the $\Sigma 7$ boundaries exhibit the highest diffusivity and $\Sigma 3$ boundaries the lowest. With increasing temperature, Si segregation at all three types of GBs increases, while the rate of change with temperature decreases in the order $\Sigma 7 > \Sigma 21 > \Sigma 3$.

6 Calculation of diffusion coefficient using parallel-replica dynamic method

The parallel-replica dynamics (PRD) method [19–21] is applied to investigate Al and Si diffusion in IPBs and other structures of the Al-Si system. This method accelerates MD simulations by exploiting parallel computing. The basic idea is to run multiple replicas of the system simultaneously on different processors to sample rare events and longer timescales.

The procedure involves the following steps:

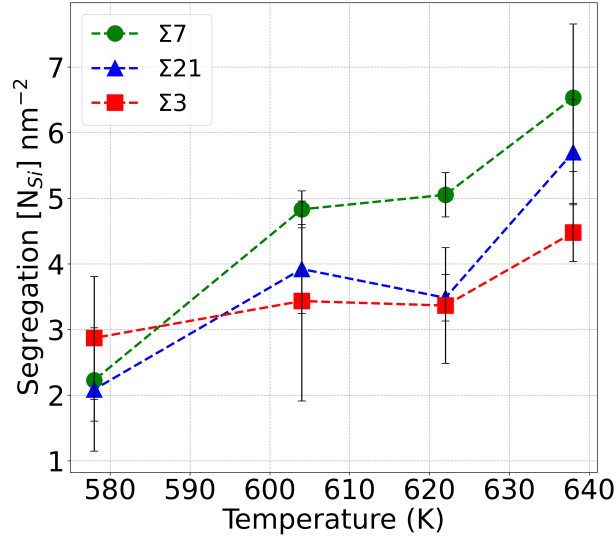


Figure S1: Si segregation at $\Sigma 3$, $\Sigma 7$, and $\Sigma 21$ grain boundaries in the Al(Si) layers deposited on the Si(111)- 1×1 substrates at temperatures ranging from 578 K to 638 K.

1. The simulation system is replicated M times, with each replica assigned to a different processor.
2. Each replica runs an independent MD simulation starting from the same initial state.
3. When any replica detects a transition, all replicas stop the simulations.
4. The system state after the transition is replicated and sent to all processors.
5. All replicas restart their simulations from this new state, and the process repeats.

By this algorithm, the PRD effectively extends the timescale of MD simulations by up to a factor of M .

In this work, we used $M = 48$ or 96 replicas, depending on the transition frequency in different structures. The MD integration time step was set to 0.0005 ps. A state transition was defined as an event in which any atom moves more than 2.5 \AA from its previous position upon energy minimization. The minimization and checks of transitions were performed every 0.05 ps. Each replica performed a dephasing step of 0.2 ps upon entering a new state to randomize the initial conditions and eliminate correlations between replicas. A correlation time of 0.25 ps was set to define the correlation between two consecutive events. The temperature of PRD simulations is controlled with the NVT ensemble.

The diffusion coefficients were calculated from the Einstein relations:

$$D_x = \frac{\langle x^2 \rangle \rho_{\text{deposition}}}{2t \rho_{\text{PRD}}} = \frac{1}{2t} \frac{\rho_{\text{deposition}}}{\rho_{\text{PRD}}} \frac{1}{N} \sum_{i=1}^{N_{\text{event}}} \sum_{j=1}^N |\Delta x_{ij}, \text{ if } |\Delta r_{ij}| > 1|^2, \quad (1)$$

$$D_y = \frac{\langle y^2 \rangle \rho_{\text{deposition}}}{2t \rho_{\text{PRD}}} = \frac{1}{2t} \frac{\rho_{\text{deposition}}}{\rho_{\text{PRD}}} \frac{1}{N} \sum_{i=1}^{N_{\text{event}}} \sum_{j=1}^N |\Delta y_{ij}, \text{ if } |\Delta r_{ij}| > 1|^2, \quad (2)$$

$$D_x = \frac{\langle x^2 \rangle}{2t} = \frac{N_{\text{event}}}{2t N_{\text{diffuse}}} \sum_{i=1}^{N_{\text{event}}} \sum_{j=1}^N |\Delta x_{ij}, \text{ if } |\Delta r_{ij}| > 1|^2, \quad (3)$$

$$D_y = \frac{\langle y^2 \rangle}{2t} = \frac{N_{\text{event}}}{2t N_{\text{diffuse}}} \sum_{i=1}^{N_{\text{event}}} \sum_{j=1}^N |\Delta y_{ij}, \text{ if } |\Delta r_{ij}| > 1|^2, \quad (4)$$

where t is the aggregate time across all replicas. Eqs. (1) and (2) calculate the diffusion coefficients of all atoms in the probe region along the X and Y directions. Eqs. (3) and (4) calculate the diffusion coefficients of only the diffusing atoms in the same probe region.

In Eqs. (1) and (2), $\rho_{\text{deposition}}$ and ρ_{PRD} denote the density of interstitials or vacancies in the system obtained by the simulated deposition process and in the respective small model created for the PRD simulations. N is the total number of Al or Si atoms in the probe region. Thus, Eqs. (1) and (2) rescale the MSD by the ratio of (i.e., $\rho_{\text{deposition}}/\rho_{\text{PRD}}$). In Eqs. (3) and (4), N_{diffuse} is the accumulated number of atoms that participate in the diffusive events (i.e., the total number of atoms that have displacements larger than 1 Å in all the events), and N_{event} is the total number of diffusive events in the PRD simulation. Thus, the term $N_{\text{diffuse}}/N_{\text{event}}$ represents the average number of diffusing atoms per diffusion event. Further, Δx_{ij} and Δy_{ij} are the displacements of the j^{th} atom in the i^{th} diffusion event along the X and Y directions, respectively, and $|\Delta r_{ij}|$ is the displacement magnitude of the j^{th} atom in the i^{th} diffusion event.

Only atoms that move more than 1 Å in the diffusion event are considered in the calculation. Because the atoms that displace less than 1 Å return to their previous positions in the subsequent event, they are assumed to be vibrating and not diffusing. This criterion works for most conditions and only fails in very rare cases, with minimal impact on the final calculation of the diffusion coefficient.

PRD simulations show that interstitials and vacancies are the major sources of diffusion in the Al(Si)/Si systems with (7×7) IPBs, which contain no other microstructure elements. Without interstitials or vacancies, few diffusion events were observed. Although the formation of Frenkel pairs can occur, the vacancy and interstitial always recombine in the subsequent event, contributing nothing to diffusion. The PRD models have much higher interstitial and vacancy densities than the deposited structures. The densities of

interstitials and vacancies in the deposited structures were computed using Wigner-Seitz defect analysis in OVITO [34]. The interstitial density in the deposited structures was found to be about 1 interstitial per 4000 atoms, while that of vacancies is about 1 vacancy per 10^5 atoms (i.e., $\rho_{\text{deposition}}$). The interstitial and vacancy density in the PRD models is around 1 interstitial or vacancy per 300 to 500 atoms, depending on specific models (i.e., ρ_{PRD}).

For each PRD model, we ran three PRD simulations starting from different initial states (i.e., different initial positions of the interstitial or vacancy in the model). We also ensured that more than 100 diffusion events occurred in each PRD simulation. The final diffusion coefficient was the average of three PRD simulations, and the error was estimated by their standard deviation.